

THE PRISM MULTI-OBJECT SURVEY (PRIMUS). II. DATA REDUCTION AND REDSHIFT FITTING

RICHARD J. COOL¹ JOHN MOUSTAKAS² MICHAEL R. BLANTON³ SCOTT M. BURLS⁴ ALISON L. COIL⁵ DANIEL J. EISENSTEIN⁶ KENNETH C. WONG⁷ GUANGTUN ZHU⁸ JAMES AIRD⁵ REBECCA A. BERNSTEIN⁹ ADAM S. BOLTON¹⁰ DAVID W. HOGG³ ALEXANDER J. MENDEZ⁵

Draft version September 12, 2018

ABSTRACT

The PRISM MUti-object Survey (PRIMUS) is a spectroscopic galaxy redshift survey to $z \sim 1$ completed with a low-dispersion prism and slitmasks allowing for simultaneous observations of $\sim 2,500$ objects over 0.18 deg^2 . The final PRIMUS catalog includes $\sim 130,000$ robust redshifts over 9.1 deg^2 . In this paper, we summarize the PRIMUS observational strategy and present the data reduction details used to measure redshifts, redshift precision, and survey completeness. The survey motivation, observational techniques, fields, target selection, slitmask design, and observations are presented in Coil et al. (2011). Comparisons to existing higher-resolution spectroscopic measurements show a typical precision of $\sigma_z/(1+z) = 0.005$. PRIMUS, both in area and number of redshifts, is the largest faint galaxy redshift survey completed to date and is allowing for precise measurements of the relationship between AGNs and their hosts, the effects of environment on galaxy evolution, and the build up of galactic systems over the latter half of cosmic history.

Subject headings: galaxies: distances and redshifts, galaxies: evolution, galaxies: high-redshift, large-scale structure of universe, surveys

1. INTRODUCTION

The PRISM Multi-object Survey (PRIMUS) is a new spectroscopic survey of faint galaxies focused on measuring the evolution of galaxy properties and large-scale structure since $z \sim 1$. PRIMUS uses a hybrid technique between very low-resolution redshifts measured from galaxy photometry and high-resolution spectroscopy. Rather than using a more traditional grating or grism, we utilize a specially designed low-dispersion prism to observe the full optical spectra of up to $\sim 3,000$ objects simultaneously. Combined with the 0.2 deg^2 field of view provided by the IMACS spectrograph on the Baade I 6.5m telescope at Las Campanas, PRIMUS spectroscopically measures galaxy redshifts in much less time than would be required with more traditional high-resolution spectroscopic techniques ($\sim 10,000$ galaxies per night) and reaches depths of $i \sim 23$ in one hour. PRIMUS redshifts have typical precision of $\sigma_z/(1+z) =$

0.005. PRIMUS spectroscopy focuses on fields with existing optical imaging for target selection and emphasizes areas with existing high-quality multiwavelength imaging from *GALEX*, *Spitzer*, *Chandra*, and *XMM-Newton*. The combination of PRIMUS redshifts with this wealth of multiwavelength data allows for detailed measurements of galaxy colors, luminosities, star formation rates, and stellar masses.

Traditional spectroscopic redshift surveys require considerable resources to be completed, especially as one probes galaxies beyond the local universe. For example, the DEEP2 survey (Davis et al. 2003) required more than 80 nights on Keck and zCOSMOS (Lilly et al. 2007) and VVDS (Le Fèvre et al. 2005; Garilli et al. 2008) utilized over one hundred VLT nights each. With this large amount of observing time, these surveys probe $\sim 20,000$ galaxies over a few square degrees. PRIMUS represents a new paradigm in galaxy redshift surveys which enables the efficient survey of large astronomical volumes with much less observation time than required with traditional higher-resolution spectroscopy. The methods pioneered by PRIMUS have already been adopted and refined for other prism spectroscopic surveys of the high-redshift universe (Kelson et al. 2012; Just et al. 2012; Gray et al. in prep).

Science with the PRIMUS dataset is ongoing. In Aird et al. (2012), we measure X-ray observations in PRIMUS fields to find evidence the presence and accretion of AGNs does not depend on the stellar masses of their host galaxies. Wong et al. (2011) investigated tidally triggered star formation in isolated close galaxy pairs and measured an enhancement in the specific star formation rate due to tidal interactions in these galaxies. We investigated optically “red and dead” galaxies which show signatures of star formation from their infrared photometry in Zhu et al. (2011) and show that a significant fraction of red-sequence galaxies have ongoing

¹ MMT Observatory, Tucson AZ 85721

² Department of Physics, Siena College, 515 Loudon Rd., Loudonville, NY 12211

³ Center for Cosmology and Particle Physics, Department of Physics, New York University, 4 Washington Place, New York, NY 10003

⁴ D.E. Shaw & Co. L.P., 20400 Stevens Creek Blvd., Suite 850, Cupertino, CA, 95014

⁵ Department of Physics, Center for Astrophysics and Space Sciences, University of California, 9500 Gilman Dr., La Jolla, San Diego, CA 92093

⁶ Harvard-Smithsonian center for Astrophysics, 60 Garden St, MS #20, Cambridge, MA 02138

⁷ Steward Observatory, The University of Arizona, 933 N. Cherry Ave., Tucson, AZ 85721

⁸ Center for Astrophysical Sciences, Department of Physics and Astronomy, Johns Hopkins University, 3400 North Charles Street, Baltimore, MD 21218, USA.

⁹ Department of Astronomy and Astrophysics, UCA/Lick Observatory, University of California, 1156 High Street, Santa Cruz, CA 95064

¹⁰ Department of Physics and Astronomy, University of Utah, Salt Lake City, UT 84112

ing obscured star formation. In Moustakas et al. (2012), we present the stellar mass function of PRIMUS galaxies and conclude that star forming galaxies are quenched more strongly with decreasing stellar mass and the majority of the stellar mass buildup within quiescent galaxies occurs around $\sim 10^{10.8} M_{\odot}$.

This paper describes the observations, data reduction, redshift fitting, redshift precision, and lessons learned from our experience with low-resolution prism spectroscopy. A companion paper (Coil et al. 2011) (hereafter Paper I) describes the survey design and characteristics and provides an overview of the data taken as part of the PRIMUS survey. The paper is outlined as follow. Section 2 outlines the details of PRIMUS observations including details of our nod & shuffle spectroscopy, calibration data, and prism characteristics. In §3, we provide a detailed discussion of our image reduction and spectral extraction including corrections due to scattered light and our wavelength calibration. We summarize our measurements of the flux corrections for our PRIMUS spectra in §4. Section 5 introduces the spectral libraries we utilize to measure redshifts from PRIMUS spectroscopy and detail the fitting algorithm. The redshift precision and outlier rates are presented in §6.1 and completeness estimates are presented in §7 before concluding in §8. The first release of PRIMUS redshifts has been completed and can be found at <http://primus.ucsd.edu>.

2. OBSERVATIONAL STRATEGY

Traditional wide area multiobject spectrographic surveys utilize either slit masks or fiber-fed spectrographs to obtain spectra for tens or hundreds of galaxies simultaneously. By replacing the traditional grism or grating dispersive element with a low dispersion prism, PRIMUS utilizes slit masks to obtain spectra for thousands of galaxies simultaneously. Figure 1 shows a mosaic for all eight IMACS CCDs for one PRIMUS science exposure illustrating the large multiplexing power available with our low-dispersion prism technique. We design each PRIMUS slitmask to provide the maximum number of high priority galaxies while also ensuring we dedicate enough slits on each mask for calibration purposes.

PRIMUS utilized existing optical photometric catalogs for target selection and mask design. Paper I details the galaxy and AGN selection criteria, mask design, sparse sampling, and photometric catalog details used in our mask design. Here, we focus on the observational and analytical methods used to obtain spectra for PRIMUS targets.

All PRIMUS spectroscopy was observed in nod & shuffle mode (Glazebrook & Bland-Hawthorn 2001) with IMACS on the Baade Magellan I telescope at Las Campanas. Figure 2 shows the PRIMUS prism resolution and dispersion as a function of wavelength. The prism resolution is a strong function of wavelength and has lowest resolution in the red. Robust sky subtraction is vital for PRIMUS redshift fitting as most galaxies are fit based on the shape of the continuum (galaxies with strong emission lines include those lines in the redshift fitting, but many galaxies in our sample have weak or absent emission lines). As nod & shuffle allows us to measure the sky flux in the same pixels as we measure object flux, we can perform robust sky subtraction.

Rather than nodding the mask such that objects moved

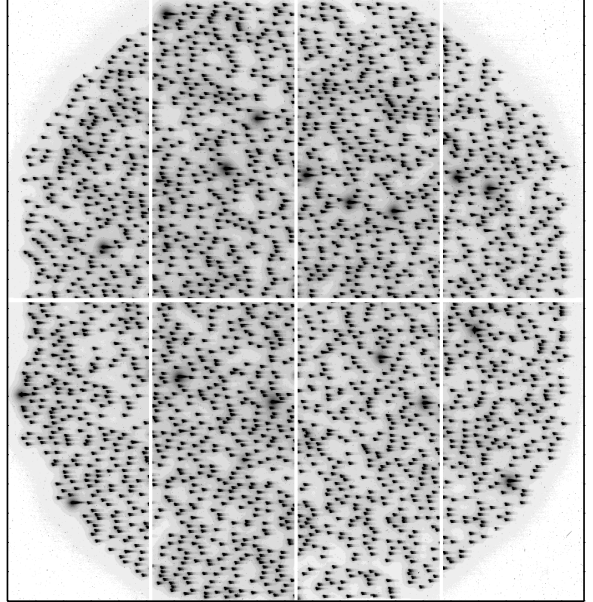


FIG. 1.— Mosaic of all eight IMACS CCDs for a single PRIMUS science exposure. Each trace of light corresponds to two individual slits which have been shuffled on the detector, resulting in 4 traces per object. The very bright traces in the image correspond to alignment stars utilized to ensure that the slitmask has been centered properly when pointing the telescope.

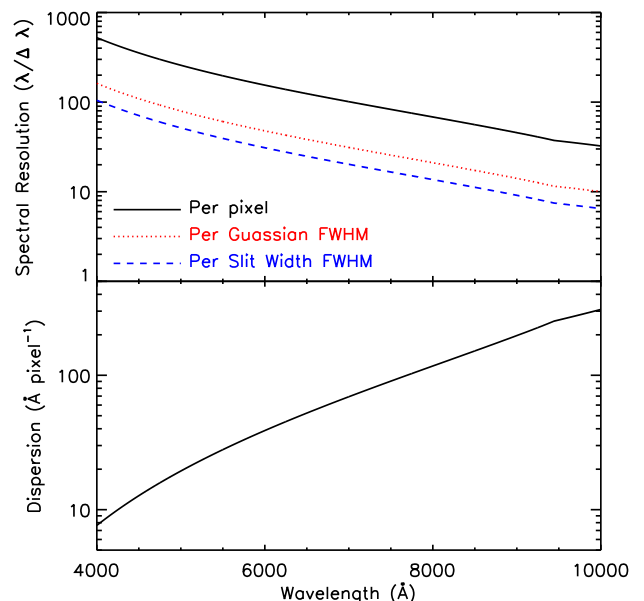


FIG. 2.— Resolution and dispersion of the PRIMUS prism versus wavelength. The resolution and dispersion generated by the low dispersion prism is a strong function of the wavelength with increased resolution in the blue but low resolution at $9000\text{\AA} - 1\mu\text{m}$. The low resolution allows us to observe the full optical spectrum of a target galaxy on only ~ 150 pixels on the detector and up to ~ 3000 galaxies on a single mask.

along one long slit, we adopted a strategy of cutting two slits (often referred to as slit A and slit B throughout this paper) for each object on the mask separated by $(\Delta\alpha, \Delta\delta) = (-1''.6, -3''.2)$ when we designed $0''.8$ wide slits and $(\Delta\alpha, \Delta\delta) = (-2''.0, -4''.0)$ when we designed $1''.0$ slits. By nodding in both directions on the sky rather than in a single direction, we minimize the impact of a bad column on the final extracted spectrum of an observed galaxy; a galaxy moved in both directions will not lose all of the information from the wavelength associated with the bad column. During each telescope nod, the detector was also shuffled 8 (10) pixels for masks with $0''.8$ ($1''.0$) wide slits. An example of nod & shuffle traces for a single object is shown in Figure 3. Due to nodding between two slits, the final observation includes four traces for each object; two traces with only sky illumination and two with both sky and object contributions. In November 2007, modifications to the IMACS instrument lead to a slight change in this layout; objects after this date were observed in the outer two traces and the inner two traces contained only sky light. Throughout this paper we will often discuss slits (either object slits or sky slits), referring to the spectrum observed through a single slit (in either object or sky position). When we discuss the “full object trace” we refer to the collection of the 4 traces shown in Figure 3 including the 2 sky traces and 2 objects traces coming from slit A and slit B in nod & shuffle mode.

Science frames were typically observed in four 16 minute nod & shuffle exposures for a total exposure time of 64 minutes (32 minutes in each nod & shuffle object slit). In COSMOS, we exposed deeper due to the wealth of high-quality data in the field; COSMOS masks included six 16 minute exposures for a total of 96 minutes per mask.

3. IMAGE ANALYSIS AND SPECTRAL EXTRACTION

We utilize a multi-stage process to first remove contamination light from the full two-dimensional science frames and then to extract the one-dimensional spectrum of each observed object. In this section, we provide the details relevant to our processing of IMACS images and the methods we utilize to obtain high-fidelity low-dispersion spectra via nod & shuffle sky subtraction. Finally, we discuss the modeling methods used to extract object spectra.

3.1. Large Scale Scattered Light

IMACS images suffer from large diffuse halos of light around bright sources. The total light contained in this halo is correlated with the flux of nearby objects and is extended enough to influence the light gathered in nearby object traces. The scattered light crosses chip gaps, indicating that the halos are not due to scattering within the CCDs themselves but are likely created in the camera optics. The presence of excess light will lead to errors in sky subtraction and can easily contaminate extracted spectra if not carefully corrected.

Figure 4 illustrates the presence of the large scale halo light near two object trace sets from a PRIMUS science exposure. On the right, we show two slices through the image; the red and blue slices are taken at the locations

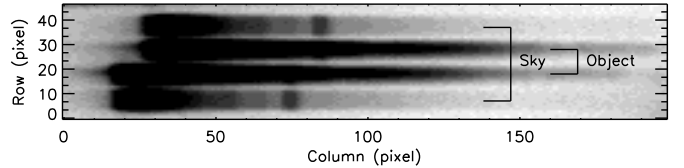


FIG. 3.— Example of a full bright-object trace from PRIMUS spectroscopy. PRIMUS observations are completed in nod & shuffle mode with the object nodded between two slits separated in both right ascension and declination. This pattern results in four traces on the final image, two traces of pure sky light and two traces of object combined with sky. In this figure, red is to the left and blue to the right. For reference, the bright sky line near pixel 73 (83) in the bottom (top) trace corresponds to 5577 Å. The resolution and dispersion of the PRIMUS prism are strong functions of wavelength; the forest of emission lines in the red portion of the spectrum are blended at PRIMUS resolution.

of the vertical red and blue lines in the two-dimensional image. The clear signal of light between the trace sets is the signature of the large scale scattering halo we characterize and remove using the details in this subsection.

In order to remove the contribution from the large-scale scattering light component, we first stack two-dimensional images of full traces with no targeted object (originally milled to characterize sky emission) and use this stacked image to create a model for the scattered light profile. We parameterize the scattered light term as a convolution of our image with kernel, $k(x, y)$

$$k(x, y) = \left(1 + \frac{x^2 + y^2}{r_0^2}\right)^{-p} \quad (1)$$

where x and y correspond to the pixel coordinates on the detector and r and p are free parameters we fit to characterize the shape of the scattered light halo.

We create a two-dimensional model for the scattered light by coadding all of the science exposures for a given pointing to increase the signal-to-noise ratio in the scattered light and remove cosmic rays. We mask the location of full traces on the coadded image and then fit for the kernel scale length, r_0 , and power-law index, p , over the full 0.2 deg^2 IMACS focal plane using the Levenberg-Marquardt method with the IDL routine `mpfit` (Markwardt 2009).

We find that a simple convolution of the best-fit kernel and the original science image is not sufficient to provide a full correction to the scattered light due to several factors. First, the amplitude of the scattered light with respect to the incident light from the slits varies as a function of position on the focal plane. Second, we find that,

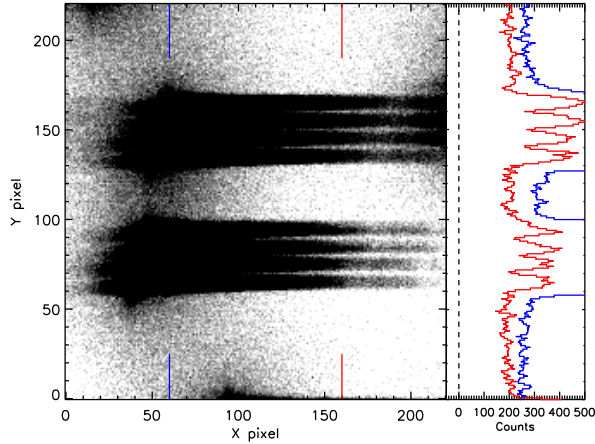


FIG. 4.— Left: Two dimensional subregion from one PRIMUS science exposure. Two object trace sets (each object set is composed of four traces) are shown. The presence of light between the two trace sets is the signature of the large scale scattered light we remove before performing object extraction from our data. The red and blue vertical lines illustrate the locations where two slices were made through the image. The slices show that this scattered light contributes several hundred counts per pixel and is a clear contaminant to our spectra. Furthermore, since the scattered light has two dimensional structure on our images, performing nod & shuffle sky subtraction without removing the contaminating signal will result in poor sky subtraction.

in detail, the large-scale halo is not circularly symmetric as assumed by equation (1). In order to obtain a better model of the scattered light, we define two non-circularly symmetric kernels based on the best fitting $k(x, y)$

$$\theta = \tan^{-1}(y/x) \quad (2)$$

$$k_1(x, y) = k(x, y) \cos(\theta) \quad (3)$$

$$k_2(x, y) = k(x, y) \cos(\theta + \pi/2). \quad (4)$$

We solve for the spatial dependence of the halo term by convolving the masked image with the three kernels to generate three halo terms

$$M_{\text{halo}} = I \otimes k \quad (5)$$

$$D_{1,\text{halo}} = I \otimes k_1 \quad (6)$$

$$D_{2,\text{halo}} = I \otimes k_2. \quad (7)$$

We then solve for the spatial variation in the halo by creating the final halo image, I_{halo} , and solving for w_i to minimize the light between object traces

$$I_{\text{halo}}(x, y) = (w_0 + w_1x + w_2y + w_3x^2 + w_4y^2) + \quad (8)$$

$$M_{\text{halo}}(w_5 + w_6x + w_7y + w_8x^2 + w_9y^2) +$$

$$w_{10}D_{1,\text{halo}} + w_{11}D_{2,\text{halo}}.$$

When applying the best fitting halo image, I_{halo} , constructed in this manner, we normalize the counts in the halo to the median counts in each individual exposure to adjust for exposure to exposure differences. Figure 5 follows Figure 4 but illustrates the same two dimensional image after the large scale halo model has been subtracted. The slices shown on the right in the figure highlights the success of this technique; little light remains between the object traces.

3.1.1. Small Scale Scattered Light

In addition to the large scale scattering halo, our IMACS spectroscopic images have a second small-scale scattering component on 5–10 pixel scales. This halo component is most apparent in the red portion of the spectra and is non-axisymmetric with respect to the light in the full traces. On average, this small scale halo light corresponds to approximately 1% of the flux of the sky. While the cause of this excess light is unknown, the local nature of the light suggests it may be due to diffusion of red light in the CCDs.

For each CCD, we first locate all full trace sets without another trace within 20 pixels. For each night of observations, we stack the two dimensional image of these isolated traces after performing a nod & shuffle sky subtraction. We then quantify the presence of excess light outside of the sky traces in the composite image. We assume the object trace experiences the same amount of scattering as the sky trace (although mirrored across the trace) and construct a final empirical model for the small scale scattered light in the spectra. In the top panel of Figure 6, we show an example of such a stacked image. The scattered light is apparent especially in the red (left side). We take the scattering light in the 7 (9) pixels (for 0.8'' (1''.0) wide slits) above the top trace and that in the 7 (9) pixels below the bottom trace, and reproduce the light for each trace based on the same nod & shuffle mode as observations. In the bottom panel of Figure 6, we show the empirical model constructed from the stacked image in the top panel. Finally, we duplicate this model for each trace on the CCD to subtract the scattering light from the image. Overall, this correction is $\sim 1\%$ of the sky and thus an important contamination to remove from our data before extracting the one-dimensional spectra.

3.2. Flatfield Correction

At this point, we have performed no flat fielding of the PRIMUS two-dimensional images. When fitting PRIMUS spectra to obtain redshifts, we are not concerned with the normalization of the spectra (which is

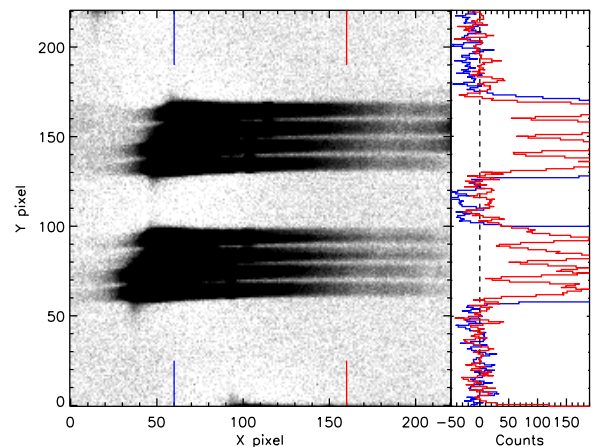


FIG. 5.— Two dimensional subregion shown in Figure 4 after the best fitting model for the large scale halo has been subtracted from the image. The slices through the image plotted on the right do not show signal between the traces.

affected by vignetting and slit losses) but removal of pixel-to-pixel changes from the detector is vital in order to not introduce false spectral features in our extracted spectra. When constructing a flat field correction for our data, we first remove any large-scale gradients present in our observed twilight sky flats. The resulting flat field measures the pixel-to-pixel variations across the detector. Since the twilight flat is observed as a single image and our science frames are observed with nod & shuffle, we cannot simply divide the science data by this pixel-to-pixel flat field correction.

Using our normalized flat-field, we construct a “nod & shuffle” corrected flat field by finding the mean between the observed flat field image and one shifted by our shuffle length. In general, PRIMUS spectra are sky-dominated, so the assumption that each nod position contributes evenly to the total contribution to the flat field is sufficient to correct all but the most severe blemishes in the flat field. Areas on the detector that are affected by flat-field corrections of more than 25% are masked as possible bad pixels and are ignored throughout the redshift fitting process to ensure that these large flat-field corrections, where our simple assumption may not be ideal, do not affect our final spectra. Less than 1% of the pixels are masked to this large flat fielding error. This final flat frame is utilized in our forward modeling of the PRIMUS science frames; in contrast to more traditionally approaches, we do not directly apply the flat field correction to our images.

3.3. Spectral Modeling & Extraction

Having corrected for the scattered light in the two dimensional images, we are ready to extract the one-dimensional object spectra from the images. In PRIMUS, we utilize a forward modeling approach to spectral extraction; we first perform an extraction without information on the spatial profile of each object. We then perform more robust extractions to construct a one dimensional profile and perform an extraction based on that profile to obtain the final extracted spectra. This section details the steps involved with calibrating the two dimensional images and extract science-quality spectra.

3.3.1. First pass extraction

We perform spectral extraction of the halo-corrected two dimensional PRIMUS spectra in a three pass method. The first pass of extraction allows us to derive the spatial profile used to extract each object, the second pass refines the sky subtraction and the final pass measures the one-dimensional extracted spectrum for each object.

In the first pass, we use a simple model for the sky and object light in order to build a more detailed spatial profile for each object in the subsequent extraction passes. Extraction is performed in a forward-modeling sense on a column-by-column basis in the images. For each column, we identify pixels associated with each PRIMUS trace. We construct models, S_i , the sky light in slit i (either slit A or slit B), and O_i , the object light in either slit position. In the first pass extraction, we construct simple models for each

$$S_i = \sum_j^{N_{\text{pix}}} w_{s,j} \delta_j f_j \quad (9)$$

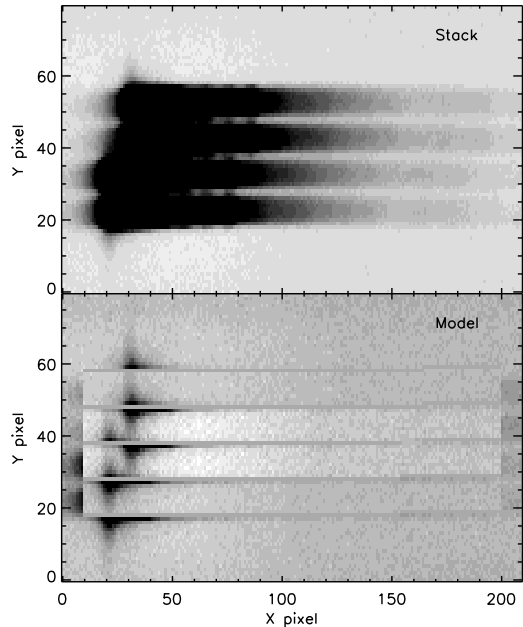


FIG. 6.— Top: Stacked image of all of the isolated traces on a single PRIMUS observation which illustrates the presence of small-scale scattered light (for examples the “spurs” of light extending above and below the traces). Bottom: Empirically constructed model used to remove the small-scale scattered light constructed as described in §3.1.1.

$$O_i = \sum_j^{N_{\text{pix}}} w_{o,j} \delta_j f_j \quad (10)$$

where f_j is the flat field contribution to pixel j in the trace, δ_j are delta-functions in each of the pixels across the trace, and $w_{s,j}$ and $w_{o,j}$ are the fluxes measured in sky and object pixels prior to the flat-field contribution. Before fitting, we construct a model for the full four trace contribution to the column from the object; the sky contributes flux only in the sky slits and both the sky and object model contribute flux in the object traces. Finally, this model is convolved with a boxcar with the width of the mask slit and a Gaussian with a 1.5 pixel width to represent the instrumental profile. By solving for $w_{s,j}$ and $w_{o,j}$, we construct a rough model for the sky and object illumination in the slit.

3.3.2. Second and third pass extractions

The second pass of extraction uses the output from the first pass in order to more robustly extract the object spectra. We start this process by generating a spatial profile of the object light in each slit. We sum the object light, as measured in the first pass, along the spectral direction of the PRIMUS trace to measure p_j , the total light in the slit as a function of pixel j across the slit. We do this sum separately for each A and B nod & shuffle position; in an ideal observation, these spatial profiles would be identical, but due to guiding errors or errors in the mask cutting, the objects may not be centered at the same pixel in both positions.

We fit p_j with a Gaussian model (solving for the centroid and Gaussian width) in order to model the spatial

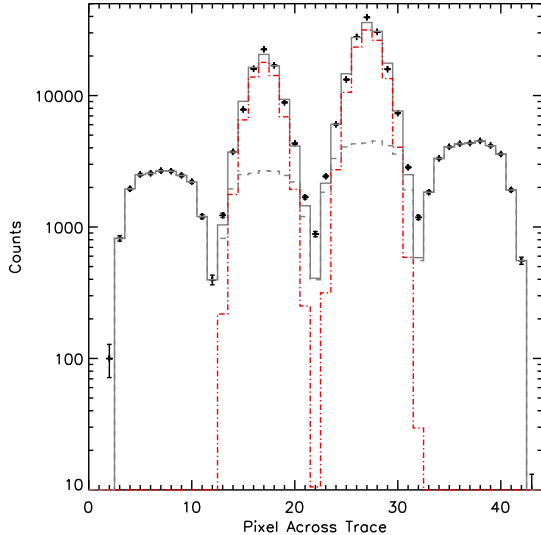


FIG. 7.— Results of the second pass of PRIMUS spectral extraction. The black data points with error bars shows the actual PRIMUS data while the red (dot-dashed) and grey denote the best fitting object and sky contributions to the four traces. The final combined model is shown by the grey line.

profile of the object. While this measurement is robust for well-detected objects in a single exposure, the lowest signal-to-noise objects have derived profiles that are heavily influenced by noise in the images. Rather than using noisy profiles for the low signal-to-noise objects, we force these objects to have the median width and centroid of the other objects on the same CCD. Based on the inferred centroid, μ_i , and profile width, σ_i , of object i , we construct a new object model

$$O_{i,j} = w_{i,j} \exp\left(-\frac{(j - \mu)^2}{\sigma^2}\right) f_j. \quad (11)$$

We perform the extraction column-by-column using this spatial profile for the object traces rather than the δ -function formulation in equation 10. Figure 7 shows a slice through one relatively bright PRIMUS object trace set. The red lines show the best fitting object profile while the blue shows the contribution from the sky. The grey line shows the sum of the sky and object models compared to the black data points with errors showing the actual PRIMUS data. We utilize the best fitting sky parameters from this pass to create a two-dimensional sky image which is subtracted from the halo-corrected two-dimensional science frame. We perform a final extraction utilizing the spatial profile derived above to extract each object trace with an optimal extraction algorithm (Horne 1986) which maximizes the signal-to-noise ratio in the extracted spectra compared to a simple boxcar extraction.

3.4. Wavelength calibration

We perform wavelength calibration using a three step process. Initially, we apply a model wavelength vector to each extracted object and sky spectrum based on the optical model for the IMACS spectrograph and PRIMUS prism. In this model, the pixels are spaced roughly evenly in λ^{-3} . Figure 8 shows the wavelength as

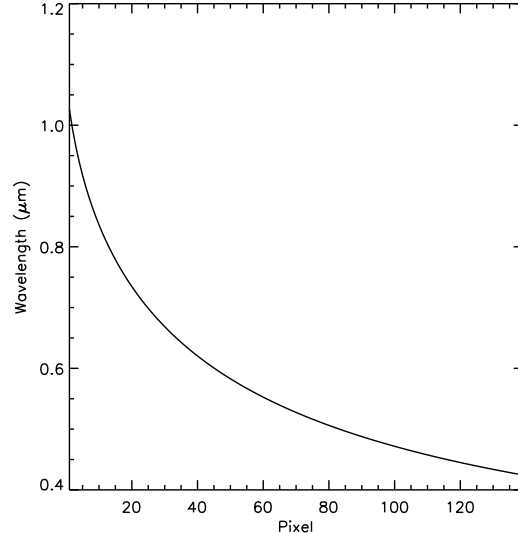


FIG. 8.— Wavelength as a function of pixel position along the trace for PRIMUS observations. This characteristic curve has pixels roughly evenly spaced in λ^{-3} . When solving for the final wavelength vector for each object in the survey, we measure the zero-point offset between this fiducial model and the observations based on the locations of key sky emission features observed in each sky slit in our nod & shuffle exposures.

a function of pixel from this optical model. In order to ensure that this model correctly constrains the final performance of the prism, we observed images illuminated by helium arc lamps on the flat field screen. We perform a simple extraction of the arc images and compare the spacing of the well-separated helium lines with the expected positions based on the prism dispersion model and find excellent agreement for all PRIMUS observing runs. Figure 9 shows one such comparison; throughout all runs, the general form of the relationship between pixel and wavelength remained fixed.

While the optical model of the instrument and prism perform well in predicting the dispersion in PRIMUS spectra, it cannot accurately predict the zeropoint for the wavelength solution on the scales needed to achieve robust redshifts. While the PRIMUS spectra are low resolution, the brightest sky lines are still readily detected and make ideal zeropoint normalizations to our wavelength solutions. Based on the strong night sky lines at 5577.34, 5895.00, 6300.3 Å, we derive a zeropoint offset for each slit on a CCD. Due to the low resolution nature of our spectra, we find the most robust zeropoints are determined by doing a cross correlation between a model sky spectrum and our observed sky in windows around each of the bright sky lines. Based on this cross correlation, we measure an offset for each object on a given PRIMUS exposure. In order to properly calibrate objects where a portion of the bright sky lines are affected by bad columns and to protect against contamination from cosmic rays which may occur if we apply a slit-by-slit zeropoint correction, we fit a low order polynomial to the the final zeropoint shifts as a function of position on the IMACS focal plane. We then apply the corresponding model value to each slit in our science observation.

The zeropoint derived from the sky lines is appropriate if the slit is filled evenly by the object or for slits

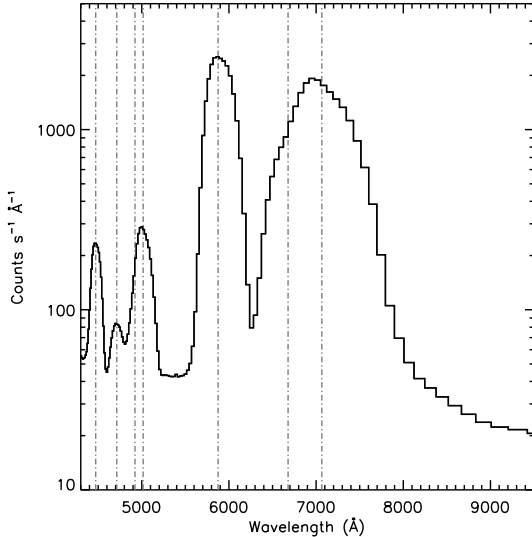


FIG. 9.— Comparison of the wavelength solution determined by using an optical model for the IMACS optical path combined with our refinement based on the location of prominent features in the sky spectrum with an extraction of a helium lamp observation through the same slit. Using a technique based on sky line features allows us to determine wavelength corrections based on simultaneous observations with our object spectra rather than extrapolating corrections from images which bracket our science frames. The location of key lines in the helium spectrum are highlighted in by dot-dashed lines.

in which the object is centered. Due to alignment errors, mask cutting errors, astrometry errors in the photometric catalog, etc, this assumption is not always true for PRIMUS observations. Ignoring the effect of non-aligned slits can lead to systematic errors in our final wavelength calibration, and thus we utilize the ~ 30 F-stars observed on each PRIMUS mask in order to derive systematic zeropoint offsets in the object spectra after the sky-line normalization has been applied. For each target F-star candidate, we fit a grid of Kurucz (1993) stellar models to the stellar photometry in order to determine an appropriate model. We convolve the best fitting stellar spectrum and measure, through a χ^2 search, any residual offset between the model and stellar wavelength model. Typically, the final shifts are small (< 0.1 pixels) and vary smoothly as a function of position on the focal plane (as one would expect if the shifts were due to alignment errors or large scale drifts in the astrometry). We fit the shifts as a function of position on the Baade focal plane and apply the zeropoint correction to each object spectrum.

3.5. Coadding Extracted Spectra

Throughout the extraction and wavelength calibration process, we work on each individual science exposure separately rather than on a coadded image of all of our exposures. Primarily, we do this to protect against guiding errors, which can accumulate from exposure to exposure, leading to systematic problems when trying to extract a coadded image. Furthermore, as we work in nod & shuffle mode, if a subset of the exposures were subject to changes in the sky brightness on timescales shorter than our nod time, these images will have systematically poor sky subtraction; including them before extracting will

lead to systematic errors in our extracted spectra.

Before coadding individual exposures, we first search for frames which do not have the quality desired to be included in the final stacked science data. If a frame was observed under conditions in which the nod & shuffle procedure fails due to sky conditions changing on timescales shorter than our nod timescale, the sky subtraction will leave residual light (or deficient light) in one object slit compared to the second. This will manifest itself both in systematic errors when the difference between the object spectra in slit A are compared to slit B, $O_A - O_B$. Furthermore, remnant sky light in the extracted spectra will lead to systematically different signal-to-noise ratios in slit A, SN_A , versus that in slit B, SN_B . We isolate any exposures with significant difference from the mean in the $< O_A - O_B >$ versus SN_A/SN_B plane and identify those exposures as possibly contaminated exposures and reject those exposures when constructed the coadded final spectra. Of the 705 science images we observed for PRIMUS, 12 exposures were rejected based on these criteria.

After any problematic exposures have been removed, we coadd the extracted one-dimensional spectra measured in each of our exposures to determine the final spectrum for each object. In order to weight by the quality of the data in each exposure (for example due to varying airmass or transparency between exposures), we weight each exposure according to the mean signal-to-noise ratio of the mask. We construct this mean signal-to-noise ratio by fitting the signal-to-noise of each object spectrum as a function of object magnitude and determine the value of this trend at $i = 21$. We do not coadd the extracted spectra from slit A and slit B in each exposure. If we were to coadd these spectra, the fact that our objects are shifted both vertically and horizontally on the IMACS focal plane means we would need to shift the two measurements spectrally in order to coadd and would result in the noise in our final coadded spectrum being correlated. While this correlation could be tracked and treated properly in the redshift fitting, we preferred to not coadd the two slits and simultaneously fit the spectrum from slit A and slit B when solving for redshifts.

After our full extraction, scattered light corrections, and nod & shuffle sky subtraction, we find that slits drilled without any objects in them show small-scale residual light. In order to correct for this residual sky-subtraction error, we coadd the extracted counts in empty slits separately in slit A and slit B for each of the eight IMACS ccds for an entire night of observations. This results in 16 wavelength-dependent corrections for each night (one for each of slit A and slit B on the 8 CCDs). We interpolate this mean residual to the wavelengths of each object in our coadded spectra and subtract it before proceeding with redshift fitting. Figure 10 shows the magnitude of this effect compared to scaled sky spectra. Overall, this effect is 1-2% of the sky flux and thus an important correction. Removing this term greatly improves the final agreement between the extracted counts in slit A compared to slit B and redshift failures rates for galaxies with known redshifts. On nights in which, primarily due to hardware problems with the mask cutting, we had too few empty slits to make these measurements we utilized the derived correc-

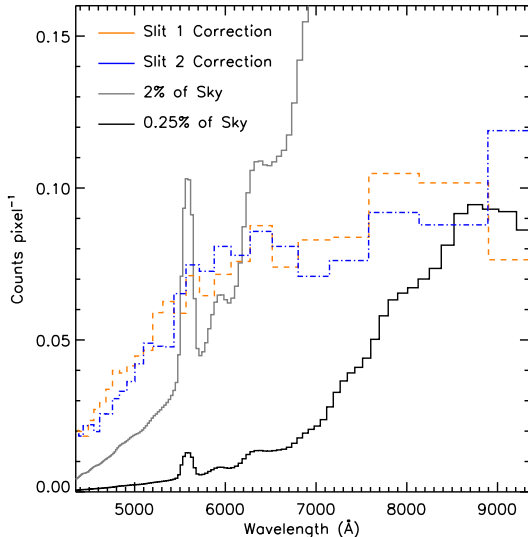


FIG. 10.— Magnitude of the residual light correction, derived by coadding the extracted spectra from slits in which no objects were observed, as a function of wavelength. The orange (dashed) and blue (dot-dashed) lines show the median correction for slit 1 and slit 2 respectively. The small scale correction contains about 1-2% of the flux of the sky and thus is an important correction when studying faint objects.

tion from the nearest night with viable data.

4. SPECTROPHOTOMETRIC CALIBRATION

Accurate spectrophotometry is essential for determining reliable redshifts for PRIMUS because our spectral resolution is too low to rely on resolve individual narrow emission lines; therefore, for many objects the redshift is largely determined by the spectral *shape* (e.g., the strength of the 4000-Å break). We emphasize that our objective is to obtain reasonably accurate *relative* spectrophotometry; the *absolute* normalization of each spectrum, which depends on the amount of light lost from the slit due to the physical extent of each object relative to the slit width, variations in the PSF, pointing errors, and so forth, is not relevant for determining the redshift with our method.

Traditionally, standard-star observations are used to derive a sensitivity function to flux-calibrate the observed spectra. By contrast, we approach the problem of spectrophotometric calibration from a forward modeling perspective. In other words, we apply our best estimate of the wavelength-dependent throughput to the *model* templates used for redshift fitting (see §5). Thus our principal goal is to determine the throughput as a function of both position on each CCD and time; we then employ the throughput estimate when fitting for redshifts.

We first utilized slitless DA white dwarf observations taken in Jan 2006 to obtain an overall throughput curve for the IMACS instrument and PRIMUS prism as shown in Figure 11. We are able to calibrate the wavelength of the extracted slitless spectrum from the broad Balmer lines present in the DA spectrum. Next, we correct the spectra for atmospheric extinction at the mean airmass of each mask utilizing the Gemini South atmospheric extinction curve. Clearly one correction curve obtained at the beginning of the survey is not appropriate to fully

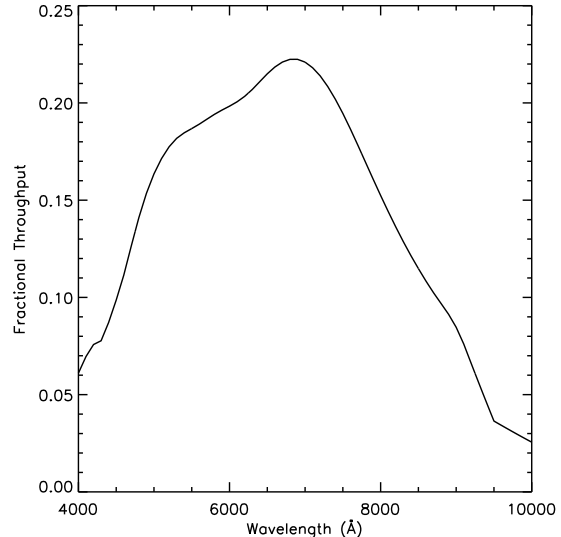


FIG. 11.— Baseline IMACS throughput used as a zeroth-order flux calibration term throughout the PRIMUS flux calibration. This curve was obtained by observing a DA white dwarf on CCD 5 of the IMACS array. The broad absorption line features allowed us to perform wavelength calibration on the slitless spectrum. We utilize the observed sky emission in each PRIMUS slit to extend the flux solution between each of the IMACS CCDs and tie each CCD to the same flux solution. We finally apply a correction based on the ~ 30 F-stars we observe on each mask to remove any variations from the overall IMACS response function over the course of the survey's operations.

calibrate our data in subsequent runs; we utilize this normalization as a baseline. More detailed corrections are applied to the data based on observations of F-stars and the night sky to remove the higher order fluxing residuals from this baseline correction.

In order to quantify how the flux correction varies between each of our PRIMUS observing runs, we utilize two tracers for the sensitivity measured on each of our PRIMUS masks. We utilize the ~ 30 F-stars on each mask to measure an average overall sensitivity function for each PRIMUS run and use the sky spectra in each mask to correct for any variations in the inter-ccd sensitivity corrections. While, in practice, we could generate mask by mask corrections, the variations between masks in a given run are small; averaged corrections allow the use of more F-star and sky measurements when constructing our fluxing terms leading to higher signal-to-noise ratio corrections.

The baseline IMACS sensitivity is tied to CCD 5 in the IMACS array. In order to normalize each of the other CCDs, we utilize the sky spectrum observed in the “off” position in our nod & shuffle observations. Based on the assumption that the sky spectrum is constant over the IMACS field of view, we measure the mean sky spectrum on each of the eight IMACS CCDs. We then measure the ratio between the mean sky measured on CCD 5 to the mean sky measured on each of the other CCDs. Figure 12 shows this procedure for one PRIMUS mask. The black spectra show the CCD 5 mean sky spectrum and the blue shows the mean for each of the other CCDs. The red line is a bspline fit utilized to remove the variation between IMACS ccds. Note that we assume the sky spectrum does not vary over the IMACS field of view. While

this is not an unreasonable assumption for the sky continuum, emission line strengths can vary on arcminute scales. The grey lines in Figure 12 illustrates this issue. As we ultimately fit a smooth bspline to the data, the few percent variations in the sky emission lines do not significantly affect our methodology. We do not expect the relative normalizations between the CCDs to be a strong function of time; by combining data over multiple masks and nights allows us to construct the highest possible signal-to-noise ratio correction. After examining the time dependence of these corrections, we chose to create these “inter-ccd” corrections for each month of PRIMUS observations. Figure 13 shows the variation with time of these correction terms. Overall, the curves for each CCD follow the same general shapes over the full course of the PRIMUS observations. Some differences arise likely due to modifications to the instrument and electronics over the course of our observations.

With each of the CCDs on the same spectrophotomet-

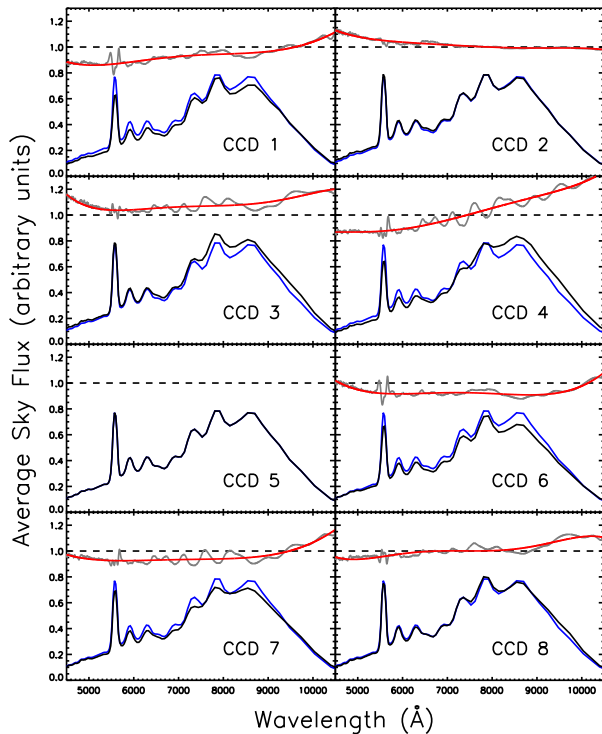


FIG. 12.— Derivation of the inter-ccd spectrophotometric corrections for one PRIMUS mask. The baseline IMACS throughput and comparison to F-stars observed on PRIMUS masks ties the PRIMUS spectra spectrophotometrically to IMACS CCD 5. Based on observations of the sky spectrum while in the “off” position in our nod & shuffle observations, we correct for the response differences between CCDs by constructing the mean sky spectrum on each CCD (blue). The ratio between this mean spectrum and the mean sky spectrum from slits on CCD 5 (black) gives a spectrophotometric correction to bring each ccd to the same system (grey). Lastly, we fit the observed ratio with a smooth bspline to characterize the low-order response variations between CCDs (red). As the temporal variation of these corrections is low, we combine observations over each month of PRIMUS observations when calculating the final inter-ccd flux correction to provide the highest signal-to-noise ratio correction possible.

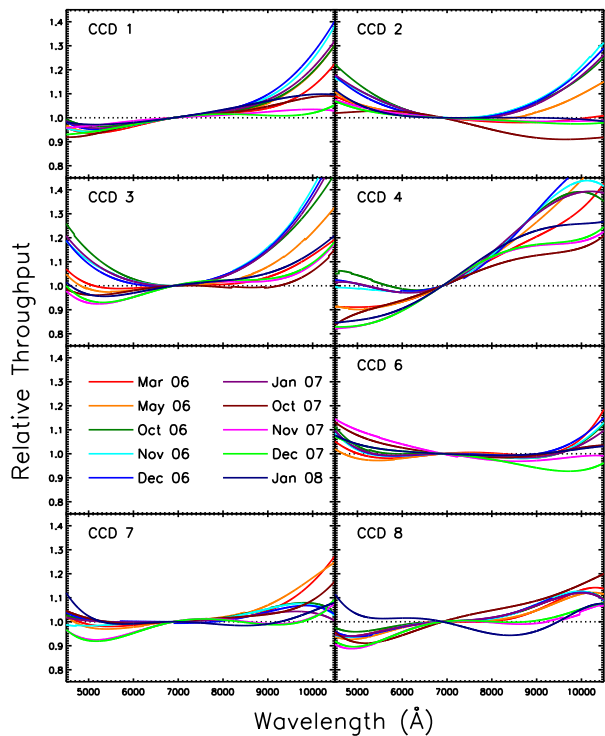


FIG. 13.— Variation of the inter-ccd flux corrections described in the text and illustrated in Figure 12 as a function of time. For each CCD, we show the final mean correction used to correct for variations between CCDs for each month of PRIMUS observations. Overall, the general form of the correction remained constant throughout the survey, but modest changes occur primarily due to instrument maintenance throughout the course of the survey.

ric system, we next bring the total spectrophotometric system of each mask onto the final survey system. While the baseline IMACS correction corrects for a general response function of the instrument, this response function can vary over time. In order to remove this variation, we utilize the ~ 30 F-stars we observed on each mask as our spectrophotometric standards. For each F-star, we fit its broadband photometry against a model of Kurucz (1993) stellar atmosphere models. We measure the ratio between the observed PRIMUS spectrum and the best-fitting stellar model which has been convolved to PRIMUS resolution. Figure 14 (a) shows this fitting process; the datapoints with errorbars show the PRIMUS data and the grey line is the convolved Kurucz (1993) model. The resulting correction vector is the ratio between the observed and model data. For each PRIMUS observing season, we combine each of these correction vectors to derive a median correction vector for the entire run as shown in Figure 14 (b). After careful comparisons, we found that the fluxing corrections within a single observing season were consistent, but corrections between seasons shows considerable variation. Figure 14 (c) shows the resulting flux corrections for each of the PRIMUS observing seasons. The changes illustrated in the figure are often physically motivated. Several major modifications were completed to the IMACS instrument throughout the course of our observing pro-

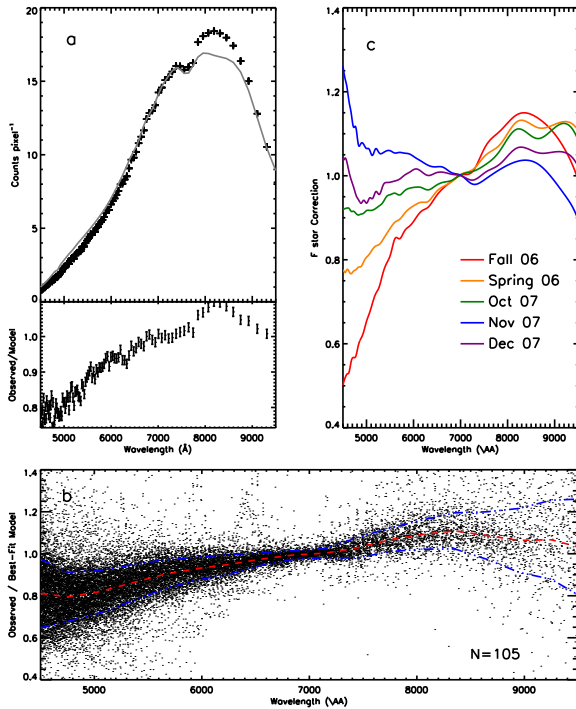


FIG. 14.— Derivation of overall flux calibration with PRIMUS F-stars. Panel a: The ratio of a PRIMUS-observed F-star (black data-points) and model F-star spectrum convolved to PRIMUS resolution (grey) is used to create the correction needed to bring PRIMUS spectra to a standard system. Panel b: To obtain the highest signal-to-noise ratio measurement of the flux calibration, we coadd the individual corrections over PRIMUS observing seasons to create the final mean correction. The raw data show the measured ratio between observed spectrum and model Kurucz (1993) spectrum. The final mean correction (red dashed line) is obtained by finding the mean of the individual corrections. The blue dot-dashed line shows the 1σ region around the mean. Panel c: The temporal variation of the F-star flux calibration vectors. Throughout the course of the survey, the IMACS team made several improvements and performed regular maintenance to the instrument – the results are clear in the increase blue sensitivity of the IMACS CCDs throughout the course of the survey.

gram to increase the throughput and sensitivity of the instrument. The corrections clearly shows that these adjustments made sizable improvements, especially at blue wavelengths.

All of these corrections correct the spectral shape of the PRIMUS spectra. The main source of small-time variation in the flux correction of our spectra which is not removed in this analysis is due to transparency variations throughout each night. These transparency variations will drive the overall normalization of our spectra high or low but will not affect the spectral shape of the spectra. When fitting our redshifts, as described in §5.3, we tie the normalization of our final model to the broadband photometry and allow the normalization of the spectra to be set by the photometric data, so transparency variations do not affect the quality of our redshift fits.

5. DETERMINING REDSHIFTS

5.1. Galaxy Spectral Templates

When fitting PRIMUS spectra, we chose to compare each PRIMUS spectrum to an empirical library of galaxy spectra in order to measure the best fitting galaxy redshift for each object. We use empirical templates, rather than a more general non-negative linear combination of spectral models. At PRIMUS resolution, fine spectral features cannot be utilized to help break degeneracies between two models which may produce similar low-resolution spectra but significantly different when viewed at higher resolution. Thus, relying on empirical galaxy templates allows us to fit our PRIMUS sample while preventing the best fitting models from occupying areas of parameters space which have no known counterparts in reality.

In order to build our empirical library of galaxy templates, we use the AGN and Galaxy Evolution Survey (AGES) galaxy sample (Kochanek et al. 2011). AGES observed 18163 galaxies with a median redshift of $z \sim 0.3$ in the NOAO Deep Wide-Field Survey Boötes field. This sample is an ideal source for our empirical templates due to the high quality spectroscopy to $I = 20.4$ and at higher redshifts than probed by lower-redshift surveys such as SDSS.

When constructing the sample of AGES galaxies to be considered in our library building, we limit the sample to galaxies with $0.05 < z < 0.35$ and only keep spectra with a mean signal-to-noise ratio of at least 4 per pixel in the AGES spectrum. This redshift range ensures that $H\alpha$ fall in the observed AGES wavelength range. Furthermore, to ensure high-quality spectrophotometry and to create a statistically complete sample, we only consider objects with $14.5 < I_{\text{Vega}} < 19.5$. We also only included AGES observations that had robust spectrophotometry. These quality cuts leave a sample of 3244 galaxies which will refer to as the “AGES parent” sample.

As the observed spectra from AGES do not extend sufficiently into the blue to cover the full observed PRIMUS wavelength range when shifted to higher redshifts, we instead use a best-fitting spectral model for the parent sample galaxies when deriving the empirical library. For each galaxy in the AGES parent sample, we perform a detailed spectral modeling of the AGES spectra simultaneously with the measured optical, GALEX, and *Spitzer* photometry. We utilize the continuum and emission line fits to AGES galaxies from Moustakas et al. (2011) when constructing the PRIMUS galaxy template set; the full details of the methods involved in the fitting of the AGES spectra can be found in Moustakas et al. (2011). The best fitting parameters were then used to construct a full UV to IR model for each AGES galaxy which is used throughout the rest of this analysis.

In order to construct a library of empirical templates from the best fitting models, we create a subsample (“basis set” hereafter) of the full AGES sample which, when convolved to the PRIMUS resolution, fully span the parent sample. To construct this sample, we first convolve each AGES sample galaxy to PRIMUS resolution assuming it was observed at $z = 0.25$. We next compute a 3244×3244 matrix from these convolved spectra; each element, c_{ij} , in this matrix is the χ^2 value calculated assuming galaxy i could be described by a simple scale factor multiplication of galaxy j in the AGES sample.

One pair of spectra can represent each other in our basis set approach if the χ^2 is smaller than a given maximum tolerance χ_{\max}^2 . Based on this matrix, we strive to determine the minimal number of AGES sample galaxies that will span the entire AGES population.

When constructing the PRIMUS basis set, we set $\chi_{\max}^2 = 2$. We then set each element in a new 3244×3244 matrix to 1 if $\chi_{i,j}^2 < \chi_{\max}^2$ and 0 if the calculated χ^2 was larger than our threshold value. We then minimize the number of columns subject to the condition that each row must have at least one element larger than 0. Mathematically, we solve

$$\min \sum_j x_j \quad (12)$$

subject to

$$\sum_j \alpha_{ij} x_j \geq 1 \quad (13)$$

where $x_j = 1$ if column j is a basis galaxy, $x_j = 0$ otherwise, and α_{ij} is the element in our binary matrix. This method results in 206 basis set galaxies.

While the galaxy models utilized to construct this basis set is complete in galaxy properties over the range of properties probed by the parent sample of AGES galaxies, the redshift limitation when constructing the AGES parent removes any information about the 2700\AA MgII emission line strengths from our basis set. To remedy this, we isolated any basis set galaxies with $^{0.1}(u-g) < 1.0$ and $EW_{[OII]} < 15$ to be possible MgII emitters based on AGES galaxies that have detected MgII emission at $0.4 < z < 0.9$ and added a second basis galaxy to the set identical to the first with the exception of the addition of a 25\AA equivalent width MgII line. This duplication is valid as we are simply seeking a set of galaxies which span the properties of galaxies at PRIMUS resolution but we do not require the minimal set of such galaxies. Figure 15 shows 15 randomly selected galaxies from the basis set used when fitting PRIMUS galaxies. As the largest source of spectral diversity in the galaxies, once convolved to PRIMUS resolution, is due to the relative strengths of optical emission lines, the basis set is primarily composed of blue star forming objects, while the red galaxy population is well sampled with only a small number of basis objects.

While our final basis set spans the full range of galaxy types in AGES when observed at PRIMUS resolution, some galaxies in this basis are much more common than others. In order to quantify this for later use in the PRIMUS redshift fitting, we utilize the basis set to fit the full AGES parent sample. For each basis galaxy, we count the number of parent galaxies that were best fit by it and record this value as the basis weight of the template, b_i . Figure 16 shows the distribution of the full AGES parent sample (small black points) and the PRIMUS basis set. The size and color of the symbols represent the basis weight of each template (redder/larger symbols show basis galaxies which characterize more parent sample galaxies at PRIMUS resolution). In both the D4000 versus $[OII]EW$ and color-magnitude parameter space, basis galaxies clearly dominate the blue/star forming portions of the diagrams; these galaxies show a large diversity in emission line strengths and continuum shapes

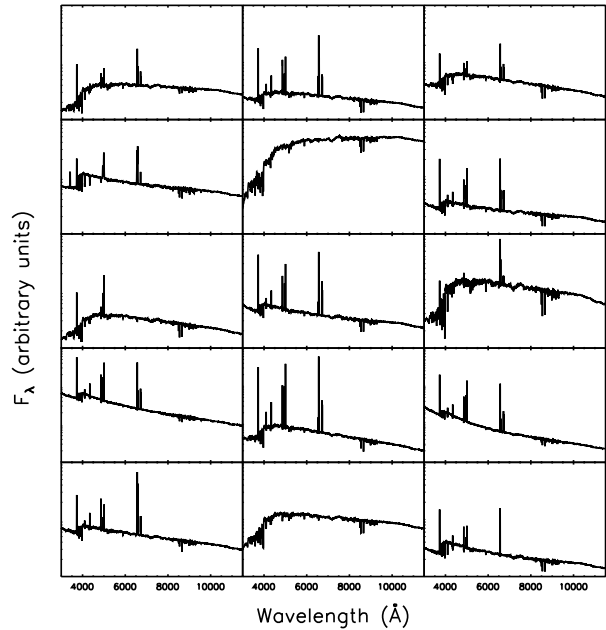


FIG. 15.— Random selection of 15 basis galaxies from the template used to fit PRIMUS spectra. Basis galaxies were selected by asking for the set of galaxies from fits to AGES objects which fully spanned the AGES galaxy sample if convolved to PRIMUS resolution. As the majority of the diversity in galaxy properties arises from emission line strengths and continuum shapes in blue galaxies, most of the PRIMUS basis galaxies are star-forming systems.

compared to more quiescent galaxies. The red/quiescent basis galaxies, on the other hand, have very high basis weights; these basis objects describe a large fraction of the AGES parent set when convolved to PRIMUS resolution.

5.2. AGN and Stellar Spectral Templates

In addition to galaxies, PRIMUS observed broadline AGNs; Paper I includes the details of the AGN selection in PRIMUS, but in brief we often did nothing to remove AGN from our galaxy sample and in some fields we actively targeted objects with color characteristic of AGNs. In order to measure redshifts for these objects and en-

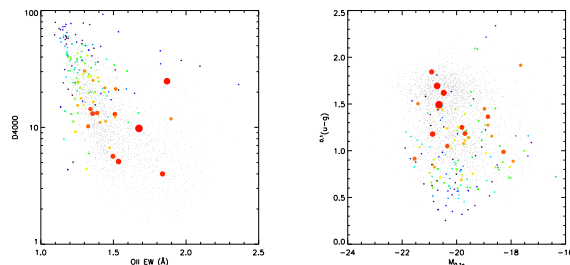


FIG. 16.— Properties of the PRIMUS basis sample (colored points) compared to the space spanned by the full AGES galaxy sample. In both panels, the color and size of data points shows the basis weight for each basis galaxy. Redder (larger) data points represent basis galaxies that can be used to represent more AGES sample galaxies when convolved to PRIMUS resolution. The vast majority of the variation in this basis set is in the blue/star forming galaxies. Left: Comparison of the strength of the 4000\AA break, D4000, with the equivalent width of $[OII]$. Right: Coverage of the PRIMUS basis galaxies in restframe color-magnitude space.

sure that only galaxies are being assigned redshifts from galactic templates, we also fit each PRIMUS object with broadline AGN templates during redshift fitting.

Obscured AGNs in which the optical spectrum has contributions from narrow emission lines from the AGN but is not dominated by broad-line emission are fit using the galaxy templates. The AGES parent sample contains examples of these Type II AGN and the stellar continuum dominates the broad shape of the spectra of these objects, and thus the galaxy templates are sufficient for determining redshifts. It should be noted, however, that due to the low resolution of PRIMUS, the presence of narrow emission lines from AGNs does not allow us to classify galaxies as AGNs. Throughout this section, we focus on creating a set of broad-line AGN templates used to classify objects which are dominated by the non-stellar AGN continuum and broad emission lines.

As a basis for our set of AGN templates, we use the SDSS composite quasar spectrum from Vanden Berk et al. (2001). While this composite contains the broad average of quasar features, the full population of AGNs have a wide range of spectral indices, α , and reddening due to dust. To span this range of parameters, we create a grid of AGN models based upon the Vanden Berk et al. (2001) composite but for which we have modified the spectral index of the AGN continuum to values of $\alpha = -2.5, -2.0, -1.5, -1.0, -0.5, 0.0$ and have included dust reddening with $E(B - V) = 0.0, 0.05, 0.1$ assuming a dust model similar to the SMC. The range of $E(B - V)$ values agrees well with the observed range of reddening observed in SDSS quasars in Hopkins et al. (2004). We find that the population of AGN in the PRIMUS sample is well spanned by these modifications in α and $E(B - V)$ and tests with broader ranges in each parameter showed the majority of PRIMUS AGN to be best fit inside the final range specified above.

In addition to the variety of continuum shapes found in AGNs, as one observes AGNs at increasingly higher redshifts, attenuation from the intergalactic medium (IGM) plays a critical role in shaping the rest-frame UV (observed optical) spectra. Neglecting this attenuation can lead to large differences between model spectra and observed AGNs at $z > 3$. With the depth probed by PRIMUS, we expect many quasars at these redshifts to be present in the sample, and thus we include a redshift-dependent attenuation from the IGM in our library of AGN template spectra based on the redshift evolution of the IGM attenuation curve presented in Madau (1995).

In addition to galaxies and AGN, the straightforward flux limit cuts in the PRIMUS target selection include galactic stellar sources as well, especially at faint magnitudes where photometric separation between stars and galaxies becomes more difficult. We utilize the empirical Pickles (1998) stellar library to create a sample of stellar templates which we compare to each observed PRIMUS spectrum in order to determine if the source is stellar in nature. Due to the low resolution of PRIMUS spectra, subtle changes in the stellar absorption features or spectral shape are not important for our application; the goal with these stellar spectra is to ensure that stellar objects are not misclassified as galaxies when we fit redshifts.

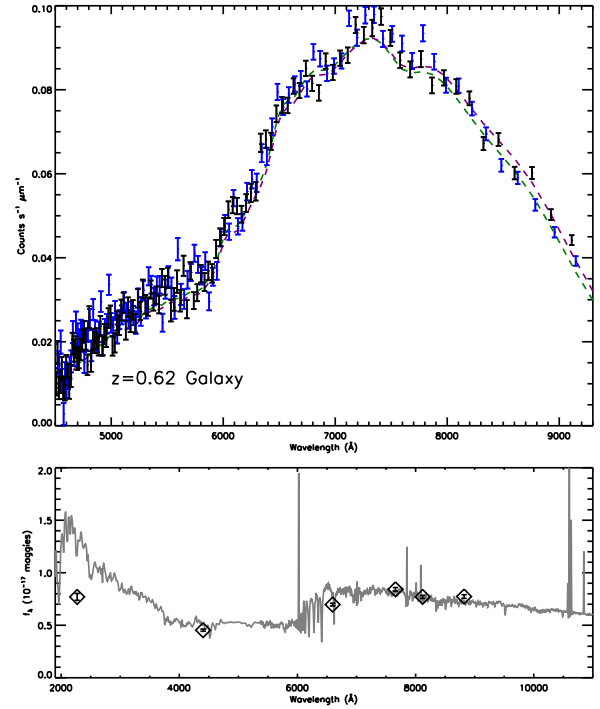


FIG. 17.— Example of a PRIMUS fit to an object identified as a $z = 0.62$ galaxy. The top panel shows the observed PRIMUS spectrum from both slit A (black) and slit B (blue). The dashed line shows the best-fitting model convolved to PRIMUS resolution. In the bottom panel, the grey line shows the full-resolution best-fitting galaxy model. The data points with errorbars mark the broadband UV and optical photometry available for the object.

5.3. Fitting Method

With the spectral template sets constructed, we perform redshift fitting of each PRIMUS object. Throughout the fitting process, we fit the slit A and slit B observations from our nod & shuffle method simultaneously. In addition to the PRIMUS spectra, we also simultaneously fit the observed optical photometry of each source. The addition of the photometry both adds information outside the spectral window of the PRIMUS spectroscopy and allows us to find the best fit in the possible presence of long-wavelength spectrophotometry errors. As we have not corrected for the large (and highly uncertain) slit losses in our PRIMUS spectra, we do not force the simultaneous fitting of the photometry and spectra to agree in absolute normalization.

When fitting galaxies, we first fit each object on a coarse grid with $\Delta z = 0.01$ spacing from $z = 0$ to $z = 1.2$. AGN are fit from $z = 0.0$ to $z = 5.0$ with 181 grid points such that the i th grid point, $z_{\text{AGN},i}$, is

$$1 + z_{\text{AGN},i} = 1.01^i. \quad (14)$$

At each grid point, we calculate the χ^2 between the measured photometry (with associated errors) and the PRIMUS spectra. When fitting, we do not give the photometry more weight than is given by the associated errors; in essence, photometry is adding ~ 6 more data

points of information to the 300 data points available from spectroscopy and thus does not dominate the fit. Due to possibility of long-wavelength spectrophotometry errors in the PRIMUS spectra, we fit each object with a model of the form

$$M(\lambda) = a_0 M_0(\lambda) (a_1 \xi(\lambda) + a_2 \xi^2(\lambda)) \quad (15)$$

where $M_0(\lambda)$ is the original template spectrum and $\xi(\lambda)$ is a refluxing vector that account for possible errors in the spectrophotometry. In detail, $\xi(\lambda)$, is a term that characterizes a linear term in $\log \lambda$

$$1 + \xi(\lambda) = 2 \frac{\log(\lambda/\lambda_{\min})}{\log(\lambda_{\max}/\lambda_{\min})}. \quad (16)$$

When performing the fits, we place priors of 10% on a_1 and a_2 ; while we expect some level of spectrophotometric errors on large-wavelength scales, we do not want the fitting to be dominated by driving the refluxing terms to unreasonable levels to compensate for actual differences between the selected model and the observed spectrum. This refluxing only applies to the comparisons between the PRIMUS spectra and convolved model. The photometry are not fitted with any form of refluxing.

Based on these fits we calculate the χ^2 between each template spectrum and the observed photometry and spectroscopy. For stars, we choose the best stellar fit to be the stellar model with the lowest χ^2 . For AGN, we choose the best fitting AGN template at each grid point by choosing the lowest χ^2 model. For galaxies, as we have information about the real frequency of each galaxy template in the full AGES parent sample. Rather than choosing the lowest χ^2 model, denoted χ_{\min}^2 , at each grid point, we calculate the effective χ^2 , χ_{eff}^2 , based on the basis weights, b_i

$$\chi_{\text{eff}}^2 = \chi_{\min}^2 - 2 \log \left(\sum_j b_j \exp \left(-\frac{\chi_j^2 - \chi_{\min}^2}{2} \right) \right). \quad (17)$$

For galaxies and AGN, we find the minimum in χ^2 versus redshift in our grid. We then fit a finer linear grid with $\delta z = 0.001$ in an interval of $|z - z_{\min}| < 0.03$ around the minimum found in the course grid, z_{\min} . Based on this finer grid, we calculate the final redshift of the galaxy or AGN as

$$z_{\text{best}} = \int z \exp \left(-\frac{\chi(z)^2 - \chi_{\min}^2}{2} \right) dz \quad (18)$$

and the associated error is the second moment of the probability distribution

$$\sigma_z = \int z^2 \exp \left(-\frac{\chi(z)^2 - \chi_{\min}^2}{2} \right) dz. \quad (19)$$

Once we have fit each PRIMUS object with galaxy, AGN, and stellar models, we must choose which of these models is the best representation of the measured data. If the final star or galaxy χ^2 is the lowest among the models, we choose to classify the PRIMUS object as a star or galaxy. After manually inspecting objects with $\chi_{\text{AGN}}^2 < \chi_{\text{gal}}^2$, including objects with known redshifts and classifications from DEEP2 and zCOSMOS, we find that

a threshold of $\chi_{\text{AGN}}^2 + 100 < \chi_{\text{gal}}^2$ provides correct redshift identification for objects that are clearly AGN (either from inspection of PRIMUS spectroscopy or previous high-resolution spectroscopy).

Figures 17, 18, and 19 show example PRIMUS fits. In each plot, the top panel shows the PRIMUS spectrum observed through slit A (black) and slit B (blue) as well as the best-fit spectrum convolved to PRIMUS resolution (dashed line). The data bars on the PRIMUS spectra are counting statistics and do not include possible systematics from sources such as flat fielding or errors in our scattered light model. The bottom panel shows the best-fitting high-resolution model as well as the broadband photometric data points available for each object (data points with errorbars).

6. REDSHIFT ACCURACY

6.1. Quality Control

Before using the PRIMUS redshifts for scientific work, it is vital to remove objects which could be contaminated due to systematics from the extraction or redshift fitting.

The majority (90% see Paper I) of PRIMUS redshifts do not change when photometry is included in the fit, however the addition of photometric measurements to the PRIMUS fits does improve the spectroscopic fits of the remaining 10%, especially at fainter magnitudes. We thus require that any robust redshift measurement from PRIMUS include at least three bands of photometry. While some of the redshifts for objects with fewer than three bands of photometry may be correct, we find the

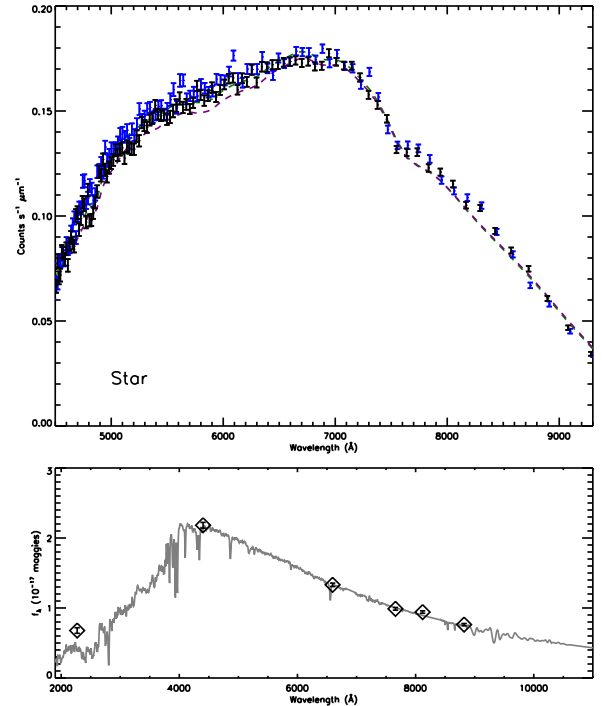


FIG. 18.— Same as Figure 17, but an example of a PRIMUS fit to an object identified as a star.

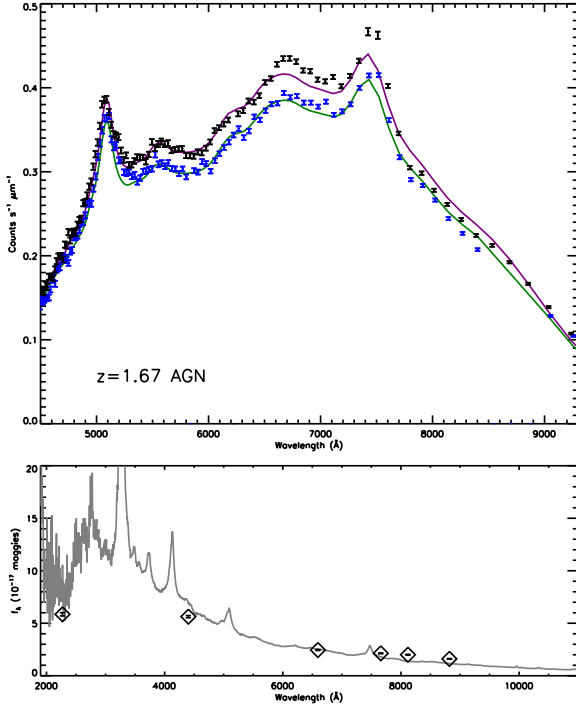


FIG. 19.— Same as Figure 17, but an example of a PRIMUS fit to a $z = 1.67$ AGN.

failure rate for objects with less than three bands of photometry is dramatically higher than for objects with more bands. Similarly, we flag any objects with more than 70% of the fitted wavelength range masked in the PRIMUS spectroscopy. These objects are predominately objects that fell near the edges of CCDs on the IMACS focal plane. Clearly, missing large sections of the object spectrum limits our ability to measure a robust redshift for these objects.

We further flag objects if the fitting of the spectrum shows signs of possible problems. If the best fitting redshift was at the extremes of the redshift range fit $z = 1.2$ for galaxies or $z = 5.0$ for AGN the object is flagged as a possible problem. If the best fitting redshift is at the extreme of the fitting range then we are unable to robustly measure a maximum in the probability distribution function. Additionally, we flag galaxies if the best fitting galaxy redshift is less than a 5σ ($\Delta\chi^2 < 25$) detection compared to other redshift minima in the grid. Typically, these are low signal-to-noise objects with very flat probability distribution functions in redshift and the minimum is a noise spike. Lastly, we flag any objects with $\chi^2 > 10^4$; these are objects for which no model in our library performed well in fitting the object and thus no redshift information from these objects is trusted.

The final test we perform checks the total available information available in the measured photometry and spectroscopy. We fit each object with a grid of powerlaw models with indices running from $\alpha = -3.0$ to $\alpha = 3.0$. If our spectra and photometry provide little information beyond a simple powerlaw model with no

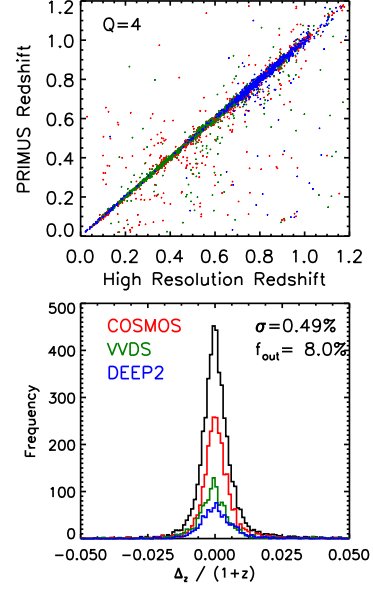


FIG. 20.— Comparison of PRIMUS redshift with redshifts obtained from higher-resolution spectroscopy from COSMOS, DEEP2, and VVDS for $Q = 4$ quality rating. The bottom panel shows the histogram of the difference between the PRIMUS and high-resolution redshift for each survey as well as the full comparison sample. Overall, we find a $\sim 0.5\%$ dispersion between PRIMUS and the high-resolution sample with $\sim 8\%$ of the galaxies falling more than 5σ from agreement.

spectral features, we do not trust the measured redshift for the object. If the best fitting powerlaw has a χ^2 of $\chi^2_{\text{best}} - \chi^2_{\text{powerlaw}} > -10$ (i.e the best fitting template model isn't better than $\sim 3\sigma$ compared to a simple powerlaw) we flag the object as suspect and remove it from our final statistical sample.

Once we have a clean sample of PRIMUS galaxies we assign each object a numerical redshift quality value. For each galaxy, we construct the statistic, ζ , which quantifies the separation of multiple minima in redshift space for each galaxy and AGN in the sample. Explicitly, we measure the difference in depths of the best and second minima in χ^2 space, $\Delta\chi^2$

$$\Delta\chi^2 = \chi^2_{2\text{nd}} - \chi^2_{\text{best}} \quad (20)$$

and calculate

$$\zeta = 1000 \frac{(\sigma_z / (1 + z_{\text{best}}))}{(\Delta\chi^2)^{1/2}}. \quad (21)$$

The numerator quantifies the width of the best peak in the $P(z)$ distribution and the denominator quantifies the separation, in a statistical sense, between the goodness of fit in the first and second minima. In extremes, if an objects has a very broad peak in $P(z)$ or if the difference in χ^2 between the first and second peaks are very close, ζ increases. We define three confidence classes based on this statistic.

$$Q = \begin{cases} 2 & \text{if } \log \zeta > 0.3 \\ 3 & \text{if } -0.3 < \log \zeta < 0.3 \\ 4 & \text{if } \log \zeta < -0.3 \end{cases} \quad (22)$$

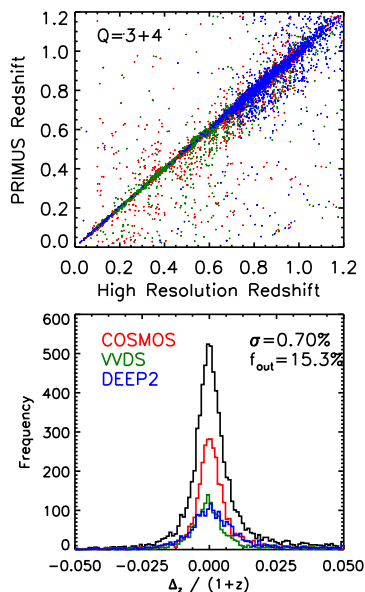


FIG. 21.— Same as Figure 20 but for galaxies with $Q = 3$ and $Q = 4$. The inclusion of $Q = 3$ adds some dispersion compared to the $Q = 4$ sample – the $Q \geq 3$ sample shows a 1σ dispersion of 0.7% and 15.3% rate of outliers more than 5σ from agreement.

The thresholds for each class are empirically determined by finding values which maximized sample completeness while minimizing outlier rate. With this classification, objects with $Q = 4$ have the most certain redshifts. For most statistical studies, a combination of $Q = 3$ and $Q = 4$ provides a sample of galaxies with confident redshifts and low outlier rate. Throughout the rest of this work, we utilize a $Q \geq 3$ sample when measuring survey completeness. Table 1 lists the scatter and outlier rate for all three quality classes as well as the fraction of the PRIMUS primary galaxy sample which were classified into each bin.

6.2. Redshift Success

In addition to the science objects observed as part of PRIMUS, we also observed targets with known redshifts in DEEP2 and VVDS fields for calibration purposes. After our initial observations, zCOSMOS released an early redshift catalog which we further use to create a sample of PRIMUS objects with known redshifts from higher-resolution spectroscopic observations. In order to quantify the redshift success from our PRIMUS observations and redshift fitting, we compare our best-fit PRIMUS redshifts to this sample of known high-resolution redshifts.

Figure 20 shows the best fitting PRIMUS redshift compared to higher-resolution spectroscopic redshifts from DEEP2, zCOSMOS, and VVDS for $Q = 4$ objects and the associated distribution of differences. Overall we find excellent agreement between the two redshift measurements with a $\sim 0.5\%$ scatter in $\Delta z / (1+z)$. Defining catastrophic outliers as objects with $\Delta z / (1+z) > 5\sigma$ we find a total outlier rate of 8%. Similarly, Figure 21 shows the same distribution for all $Q = 3$ and $Q = 4$ galaxies. We find a 0.7% scatter rate and 15% outlier rate. The

$Q \geq 3$ sample is the best suited for statistical studies of galaxy properties as it is more complete.

One of the largest sources of error in PRIMUS redshifts is the presence of degeneracies between two model spectra at different redshifts. At PRIMUS resolution, a galaxy at $z > 0.7$ with a strong 4000 Å break can be difficult to differentiate from a bluer galaxy with a Balmer break and a strong [O II] emission line at slightly higher redshift. The addition of high-quality photometry can help break this degeneracy, especially in the U-band. As an example of the aid that U-band photometry can provide to our fits, in regions with U-band photometry, we find a 25% tighter relation between high-resolution redshift and PRIMUS redshift and the number of outliers located more than 5σ from the one-to-one relationship dropped by a factor of two.

7. SURVEY COMPLETENESS

Regardless of the effort invested into any wide-area, deep, galaxy redshift survey, 100% of the objects of interest will not yield redshifts. incompleteness can arise at many phases of the survey process; galaxies may not be present in photometric catalogs due to catalog depth, technical limitations or survey time limitations may prevent the targeting of every galaxy selected as a possible target from photometric imaging, and finally observed spectra may fail to provide a reliable redshift measurement. Proper use of data obtained from galaxy redshift surveys requires the careful correction for these sources of incompleteness in order to not bias statistical analysis of the sample. As the photometric catalogs we target from in PRIMUS are often significantly deeper than the PRIMUS spectroscopic depth, we assume the incompleteness in the photometric catalogs to be negligible and focus on targeting and redshift incompleteness in the PRIMUS observations. When selecting targets for PRIMUS spectroscopy, we applied two *a-priori* sparse sampling criteria (see Coil et al. (2011) for more details). In order to ensure that the faintest galaxies, which dominate the photometric catalog, do not dominate the PRIMUS target selection, we define two bins in flux. Galaxies more than 0.5 mag brighter than the flux limit of the PRIMUS selection were sampled at a rate of 100% while galaxies below this limit were sampled at a rate of 30%. As this sparse sampling is performed during target selection and the sparse sampling weights were saved, we can correct for the magnitude-dependent sparse sampling exactly. Secondly, PRIMUS target selection utilized a density-dependent sparse sampling approach to ensure that galaxies in (projected) dense regions were not undersampled. We can upweight each galaxy by the inverse of the sparse-sampling weight to reconstruct the full magnitude-limited sample.

When designing slit masks for PRIMUS observations, not every object selected as a PRIMUS target can be observed due to slit collisions between PRIMUS targets themselves and between targets and higher priority targets such as alignment stars and flux calibration stars. The effect of these slit collisions is minimized by observing two slit masks at each PRIMUS field center and by using density-dependent sampling, but this does not allow us to observe every possible PRIMUS target. In order to correct for missing targets from slit collisions, we calculate the number of PRIMUS galaxies which were

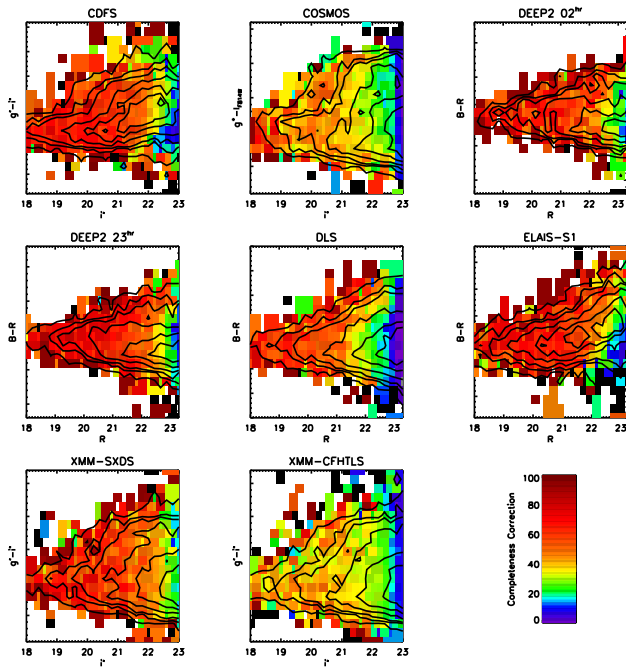


FIG. 22.— Redshift success as a function of color and magnitude for each of the PRIMUS fields. Contours enclose 25%, 50%, 75%, 90%, and 99% in the targeted PRIMUS sample while the colored background shows the fraction of targeted galaxies with a well-measured ($Q \geq 3$) redshift in PRIMUS. Due to the inhomogeneous filter systems utilized in the optical imaging across each field, we utilize synthesized $r-i$ color and i -band magnitude based on k correct fits to the observed photometry in this comparison. Overall, the primary factor in our redshift success rate is the i -band flux of the object; little trend is seen with respect to an object's color. The average redshift success is $> 75\%$ brighter than $i = 21$ and declines to $\sim 45\%$ at $i \sim 22.5$.

observed and divide by the number of PRIMUS galaxies available as a function of the number of masks each object had the opportunity to be observed on and the number of potential conflicting galaxies, N_c . Averaging over all of the PRIMUS fields except XMM-SXDS, our completeness in areas observed by two masks is 97% for $N_c \leq 2$ and declines with increases N_c to 82% for $N_c = 6$. In areas covered by four masks (in regions of the COSMOS field), our average completeness is 98% for $1 < N_c < 4$ and declines slightly to 94% for $N_c = 6$. In XMM-SXDS, we observed a factor of two more F-stars per mask than our other fields, which leads to lower overall completeness (96% for $N_c = 2$ and 75% for $N_c = 6$).

Finally, we must correct for galaxies which were observed by PRIMUS but for which we were unable to measure a reliable (defined as $Q \geq 3$, here) redshift. In order to quantify this incompleteness and explore its dependence on galaxy type, we count the number of observed galaxies as a function of both observed magnitude and color. As the photometric systems between each of the imaging datasets used for target selection used different filter sets, the exact filters used for this comparison are different between fields. In general, we choose either the i or R bands when quantifying trends with magnitude and choose a color with a large lever arm across the optical spectrum (typically $g-i$ or $B-R$) when looking at trends with observed-frame color. We then derive the final spectroscopic weight in this binned color-magnitude space. We define the final weight as the total number

of galaxies in a bin with robust redshift measurements divided by the *effective* number of galaxies (that is the total of the PRIMUS statistical weights) from the full primary sample in the bin. We use this method to ensure that galaxies from populations with few successful redshift measurements are still given full weight in the final primary sample. Figure 22 shows the completeness for each of the PRIMUS fields. In each panel the contours show the concentration of objects in the color-magnitude plane and denote 25%, 50%, 75%, 90%, and 99% of the population. The color denotes the fraction of observed PRIMUS objects which received a reliable redshift measurement. In general, the flux of the object is the dominant variable when describing the PRIMUS redshift incompleteness – little variation is seen in the completeness as a function of color at fixed flux. The average redshift success is $> 75\%$ for galaxies brighter than $i = 21$ and declines to $\sim 45\%$ at $i = 22.5$.

8. CONCLUSIONS

PRIMUS has completed observations of 185,105 galaxies with a low-dispersion prism over 9.1 deg^2 suitable for statistical investigations of galaxy evolution since $z \sim 1$. In our primary sample of galaxies with redshift measurements suitable for statistical work, PRIMUS includes 130,000 galaxies with typical redshifts errors of $\sigma_z/(1+z) = 0.005$ when compared to higher-resolution spectroscopic redshift measurements. PRIMUS is the largest faint galaxy survey completed to date. The high targeting fraction ($\sim 80\%$) and large survey volume allow for precise measurements of galaxy properties and large-scale to $z \sim 1$. In Coil et al. (2011), we summarize the motivation, observational techniques, target selection, slitmask design, and provided details of the PRIMUS observations. In this paper, we detail the data processing, spectral extraction, redshift fitting, and survey completeness of the PRIMUS.

The dramatic increase in multiplexing ability added when using the low-dispersion prism technique developed for PRIMUS compared to more traditional spectroscopic techniques at higher-resolution allows for a very efficient mapping of large areas of the sky using only a fraction of the observing time. The value of high-efficiency spectroscopic follow up will increase as the next generation of large area deep sky surveys such as the Dark Energy Survey and LSST begin providing public data. The volumes probed by these imaging surveys will be impossible to fully spectroscopically probe using traditional techniques.

While the prism technique has many strengths, especially in terms of survey efficiency, it has several limitations; the effect of these limitations can be minimized through proper planning and careful survey design. As much of the spectral information on small scales (absorption and emission lines features) will be unresolved with prism spectroscopy, the more information available to break degeneracies in spectral fitting will result in more precise redshift measurements. For example, in PRIMUS, a spectral break at $z > 0.7$ may arise due to a strong 4000 \AA break in a red galaxy or a Balmer break with an unresolved $[\text{O II}]$ emission line in a star forming galaxy. The addition of external photometry, especially in the U -band, helps to break this degeneracy. Having broadband photometry which spans the optical spectrum

provides significant improvement to redshift fits.

Traditional higher-resolution spectroscopic surveys often utilize sky fibers, extended slits, or nod & shuffle procedures to characterize the sky emission in target spectra as the signal from targets of interest are many orders of magnitude fainter than the sky and thus any contaminating emission not removed will bias the final extracted spectra. This problem is magnified with low dispersion spectroscopy as the entire trace of objects of interest may only be a few hundred pixels of information. Small scale errors that may affect only a small portion of the spectrum in high-resolution spectroscopic work (and which can easily be masked out when fitting for redshifts) removes a significant fraction of the spectral information at lower-resolution. Robust sky subtraction is essential, though the most effective technique is strongly dependent on the instrument, goals, and depth of each survey.

A key problem that required significant effort to correct in our PRIMUS observations was contamination of our spectra from large-scale scattered light in the final images. This scattered light is likely insignificant for the majority of users of the instrument as it exists on large enough scales to be removed when subtracting sky emission in direct imaging. The scattered light being dependent on the flux from nearby pixels means that most traditional high-resolution spectroscopy applications will likely be minimally effected as the counts per pixel are often significantly smaller than when working with low-dispersion spectra (as the sky emission is resolved rather than being unresolved in the red). This underlines the critical importance in understanding the instrument and optical system when performing low-resolution spectroscopic work. Often corrections unneeded, or even unnoticed, in more traditional applications will play an important role in the final success of the survey.

Once a characterization of the available photometric data, a coherent plan to remove contaminating emission from object spectra, and a firm understanding of the instrument and optical systems involved have been established, low-resolution spectroscopic surveys provide very efficient means to observed thousands of objects simultaneously. Early success with PRIMUS led to a number of current prism surveys to probe different areas of parameter space including the high redshift universe, the nature of galaxy cluster members, and the properties of colliding galaxy clusters.

This paper includes data gathered with the 6.5 meter Magellan Telescopes located at Las Campanas Observatory, Chile. We thank the support staff at LCO for their help during our observations, and we acknowledge the use of community access through NOAO observing time. Some of the data used for this project is from the CFHTLS public data release, which includes observations obtained with MegaPrime/MegaCam, a joint project of CFHT and CEA/DAPNIA, at the Canada-France-Hawaii Telescope (CFHT) which is operated by the National Research Council (NRC) of Canada, the Institut National des Science de l'Univers of the Centre National de la Recherche Scientifique (CNRS) of France, and the University of Hawaii. This work is based in part on data products produced at TERAPIX and the Canadian Astronomy Data Centre as part of the Canada-France-Hawaii Telescope Legacy Survey, a collaborative project of NRC and CNRS. Funding for PRIMUS has been provided by NSF grants AST-0607701, 0908246, 0908442, 0908354, and NASA grant 08-ADP08-0019. RJC was supported by NASA through Hubble Fellowship grant HF-01217 awarded by the Space Telescope Science Institute, which is operated by the Associated of Universities for Research in Astronomy, Inc., for NASA, under contract NAS 5-26555.

REFERENCES

- Aird, J., Coil, A. L., Moustakas, J., et al. 2012, *ApJ*, 746, 90
 Coil, A. L., Blanton, M. R., Burles, S. M., et al. 2011, *ApJ*, 741, 8
 Davis, M., Faber, S. M., Newman, J., et al. 2003, in *Society of Photo-Optical Instrumentation Engineers (SPIE) Conference Series*, Vol. 4834, *Society of Photo-Optical Instrumentation Engineers (SPIE) Conference Series*, ed. P. Guhathakurta, 161–172
 Garilli, B., Le Fèvre, O., Guzzo, L., et al. 2008, *A&A*, 486, 683
 Glazebrook, K., & Bland-Hawthorn, J. 2001, *PASP*, 113, 197
 Gray et al. in prep
 Hopkins, P. F., Strauss, M. A., Hall, P. B., et al. 2004, *AJ*, 128, 1112
 Horne, K. 1986, *PASP*, 98, 609
 Just et al., D. 2012, ph.D. Thesis
 Kelson, D. D., Williams, R. J., Dressler, A., et al. 2012, *ArXiv e-prints*
 Kochanek, C. S., Eisenstein, D. J., Cool, R. J., et al. 2011, *ArXiv e-prints*
 Kurucz, R. L. 1993, in *Astronomical Society of the Pacific Conference Series*, Vol. 44, *IAU Colloq. 138: Peculiar versus Normal Phenomena in A-type and Related Stars*, ed. M. M. Dworetzky, F. Castelli, & R. Faraggiana, 87
 Le Fèvre, O., Vettolani, G., Garilli, B., et al. 2005, *A&A*, 439, 845
 Lilly, S. J., Le Fèvre, O., Renzini, A., et al. 2007, *ApJS*, 172, 70
 Madau, P. 1995, *ApJ*, 441, 18
 Markwardt, C. B. 2009, in *Astronomical Society of the Pacific Conference Series*, Vol. 411, *Astronomical Data Analysis Software and Systems XVIII*, ed. D. A. Bohlender, D. Durand, & P. Dowler, 251
 Moustakas, J., Zaritsky, D., Brown, M., et al. 2011, *ArXiv e-prints*
 Moustakas et al., J. 2012, submitted to *ApJ*
 Pickles, A. J. 1998, *PASP*, 110, 863
 Vanden Berk, D. E., Richards, G. T., Bauer, A., et al. 2001, *AJ*, 122, 549
 Wong, K. C., Blanton, M. R., Burles, S. M., et al. 2011, *ApJ*, 728, 119
 Zhu, G., Blanton, M. R., Burles, S. M., et al. 2011, *ApJ*, 726, 110

TABLE 1
PRIMUS REDSHIFT CONFIDENCE CLASSES

Class	$\sigma_{\delta z/(1+z)}$	Outliers ^a	Sample Fraction ^b
4	0.005	7.85	49.2
3	0.022	5.32	21.6
2	0.050	5.06	29.2

^a Fraction of objects with known redshifts deviating more than 5σ from agreement.

^b Fraction of PRIMUS primary galaxies which received the specified class designation.